Cavity identification using 3-D elastodynamic BEM, shape sensitivity and topological derivative

Marc Bonnet, Bojan B Guzina, Sylvain Nintcheu Fata

CAVITY IDENTIFICATION USING 3-D ELASTODYNAMIC BEM, SHAPE SENSITIVITY AND TOPOLOGICAL DERIVATIVE

M. BONNET

Laboratoire de Mécanique des Solides (UMR CNRS 7649), Ecole Polytechnique, F-91128 Palaiseau Cedex, France
E-mail: bonnet@lms.polytechnique.fr

B. B. GUZINA AND S. NINTCHEU FATA

Dept. of Civil Engineering, University of Minnesota, Minneapolis, MN 55455, USA
E-mail: guzina@wave.ce.umn.edu

The problem of mapping underground cavities from surface, i.e. using non-intrusive seismic measurements, is investigated via a regularized boundary integral equation method. With the ground modeled as a three-dimensional uniform, isotropic elastic half-space, the inverse analysis of seismic waves scattered by a three-dimensional void is formulated as a task of minimizing a cost function involving the misfit between experimental observations and theoretical (i.e forward) predictions. This conventional choice of setting is dictated by the very high computational cost of solving the forward elastodynamic scattering problem, which makes e.g. global search strategies infeasible. For an accurate treatment of the gradient search technique employed to solve the inverse problem, derivatives of the predictive boundary element model with respect to the cavity parameters are evaluated using an adjoint problem approach. Here as in most situations where conventional descent methods (here the quasi-Newton algorithm with BFGS formula) are used, results depend on the choice of initial guess and occasional lack of convergence occurs. This has prompted the authors to investigate the use of topological derivative as a tool for preliminary probing. The topological derivative field is computed via a relatively inexpensive procedure, and appears to yield useful indications as to the topology and approximate location of the cavity system. Numerical examples are included to illustrate the effectiveness of the various steps developed so far.

Introduction. Three-dimensional imaging of cavities embedded in a semi-infinite solid using elastic waves is a topic of intrinsic interest in a number of applications ranging from nondestructive material testing to oil prospecting and underground object detection. In situations when detailed mapping of

buried objects (defense facilities, buried waste) is required and only a few measurements can be made, the use of surface discretization-based boundary integral equation (BIE) techniques provides the most direct link between the surface measurements and the buried geometrical objects. While such an approach is well established for acoustic problems [2], limited attention has so far been paid to the use of BIE methods in wave-based sensing of elastic solids. This communication reports the development of an analytical and computational framework for the identification of cavities in a semi-infinite solid from surface seismic measurements via an elastodynamic BIE method, as well as preliminary results on the investigation of the usefulness of the topological derivative (e.g. for choosing the initial guess).

Formulation and solution technique. The focus of this study is the inverse scattering problem, in the framework of linear elastodynamics in the frequency domain (with the implicit time factor $e^{i\omega t}$ omitted thoroughout) for an isotropic, homogeneous elastic half-space housing an internal void. With reference to a Cartesian frame $\{O;\xi_1,\xi_2,\xi_3\}$, the half-space $\Omega = \{(\xi_1,\xi_3,\xi_3)|\xi_3 > 0\}$ is characterized by the Lamé's constants λ and μ, mass density ρ, and is bounded on top by the free surface $S = \{(\xi_1,\xi_2,\xi_3)|\xi_3 = 0\}$. The cavity inside the half-space occupies a simply connected finite region $\Omega_c \subset \Omega$ bounded by a piecewise smooth closed surface Γ; the normal to Γ directed towards the interior of Ω_c will be denoted by $\boldsymbol{n}$. The cavity is 'illuminated' by a time-harmonic seismic source, with the resulting surface motion monitored over a finite set of slightly embedded control points $\boldsymbol{\xi} = \boldsymbol{x}^m$ $(m = 1, 2, \ldots M)$.

The total elastic displacement field $\boldsymbol{u}$ is governed by the boundary integral equation

$$\frac{1}{2}u_k(\boldsymbol{x}) + \mathrm{PV}\int_\Gamma \hat{\sigma}^k_{ij}(\boldsymbol{\xi},\boldsymbol{x};\omega)n_j(\boldsymbol{\xi})u_i(\boldsymbol{x})\,\mathrm{d}S_\xi = u^F_k(\boldsymbol{x}) \qquad (\boldsymbol{x}\in\Gamma) \qquad (1)$$

(its regularized form [5] being used in the implementation) with the free-field defined by

$$u^F_k(\boldsymbol{x}) = \int_\Omega f_i(\boldsymbol{\xi})\hat{u}^k_i(\boldsymbol{\xi},\boldsymbol{x},\omega)\,\mathrm{d}S_\xi$$

The fundamental solution (displacement $\hat{\boldsymbol{u}}^k$, stress $\hat{\boldsymbol{\sigma}}^k$) satisfies the traction-free condition $\hat{\boldsymbol{\sigma}}^k.\boldsymbol{n} = \boldsymbol{0}$ on S. Then, the displacement at sensor locations is given by the representation formula:

$$u_k(\boldsymbol{x}^m) = u^F_k(\boldsymbol{x}^m) - \int_\Gamma \hat{\sigma}^k_{ij}(\boldsymbol{\xi},\boldsymbol{x}^m;\omega)n_j(\boldsymbol{\xi})u_i(\boldsymbol{\xi})\,\mathrm{d}S_\xi \qquad (\boldsymbol{x}^m\in S) \qquad (2)$$

Inverse problem. The inverse problem of cavity identification is set here as the minimization of the least squares misfit function

$$\mathcal{J}(\Gamma) = \sum_{1\le m\le M} \frac{1}{2}\overline{(\boldsymbol{u}(\boldsymbol{x}^m)-\boldsymbol{u}^{\rm obs}(\boldsymbol{x}^m))}\cdot\boldsymbol{W}\cdot(\boldsymbol{u}(\boldsymbol{x}^m)-\boldsymbol{u}^{\rm obs}(\boldsymbol{x}^m)), \quad (3)$$

where $\boldsymbol{u}$ is the solution of the direct problem (and thus of course depends on Γ) and the over-bar symbol denotes the complex conjugation. In view of the significant computational effort required to evaluate $\boldsymbol{u}$ for elasto-dynamic problems, the minimization of $\mathcal{J}$ is here performed by means of a gradient-based quasi-Newton method with the BFGS updating formula. The gradients are evaluated from the analytical formula

$$\overset{*}{\mathcal{J}}(\Gamma) = \mathrm{Re}\Big[\int_\Gamma \Big\{\rho\omega^2\bar{\boldsymbol{u}}\cdot\boldsymbol{u} - \frac{2\lambda\mu}{\lambda+2\mu}(\mathrm{div}_S\bar{\boldsymbol{u}})(\mathrm{div}_S\boldsymbol{u}) - \mu(\nabla_S\bar{\boldsymbol{u}}+\nabla_S^T\bar{\boldsymbol{u}}):\nabla_S\boldsymbol{u} + \mu(\boldsymbol{n}\cdot\nabla_S\bar{\boldsymbol{u}})\cdot(\boldsymbol{n}\cdot\nabla_S\boldsymbol{u})\Big\}\theta_n\,\mathrm{d}S\Big] \quad (4)$$

where θ_n denotes the normal transformation velocity of Γ associated with a given parameter perturbation, and $\bar{\boldsymbol{u}}$ is the adjoint solution governed by the integral equation [1,5]:

$$\frac{1}{2}\bar{u}_k(\boldsymbol{x}) + \mathrm{PV}\int_\Gamma \hat{\sigma}_{ij}^k(\boldsymbol{\xi},\boldsymbol{x};\omega)n_j(\boldsymbol{\xi})\bar{u}_i(\boldsymbol{x})\,\mathrm{d}S_\xi = \sum_{1\le m\le M} W_{ij}^m\overline{(u_j(\boldsymbol{x}^m)-u_j^{\rm obs}(\boldsymbol{x}^m))}\bar{u}_i^k(\boldsymbol{\xi},\boldsymbol{x}^m,\omega)\,\mathrm{d}S_\xi \qquad (\boldsymbol{x}\in\Gamma) \quad (5)$$

Computational treatment and results. The boundary element solution of (1) is implemented in a standard fashion. In this investigation, eight-node quadratic boundary elements are used. The location and shape of Γ is taken to depend on a finite set of design parameters: $\boldsymbol{\xi} = \boldsymbol{\xi}(\boldsymbol{p})$, with $\boldsymbol{p} = (p_1, p_2, \ldots, p_D)$. With such assumption, the sensitivities $\partial\mathcal{J}/\partial p_d$ required for the minimization of $\mathcal{J}$ can be obtained by setting $\theta_n = \partial\boldsymbol{\xi}/\partial p_d\cdot\boldsymbol{n}$ in (4). As long as the topological characteristics of Γ are independent of $\boldsymbol{p}$, the evolving boundary element mesh representing $\Gamma(\boldsymbol{p})$ can be created by interpolating the parameter-dependent nodes $\boldsymbol{x}^q(\boldsymbol{p})$ with fixed, i.e. pre-defined, mesh connectivity.

Cavity mapping. Figure 1 illustrates the iterative process of finding an ellipsoidal cavity defined by $\boldsymbol{p}^{\rm true} = (-4a, -2a, 4a, 1.8a, 0.9a, 0.6a)$, starting from the initial guess $\boldsymbol{p}^0 = (-1.5a, -0.5a, 5a, a, a, a)$ (the cavity is parameterized in terms of its centroid coordinates c_i and semi-axes lengths α_i,

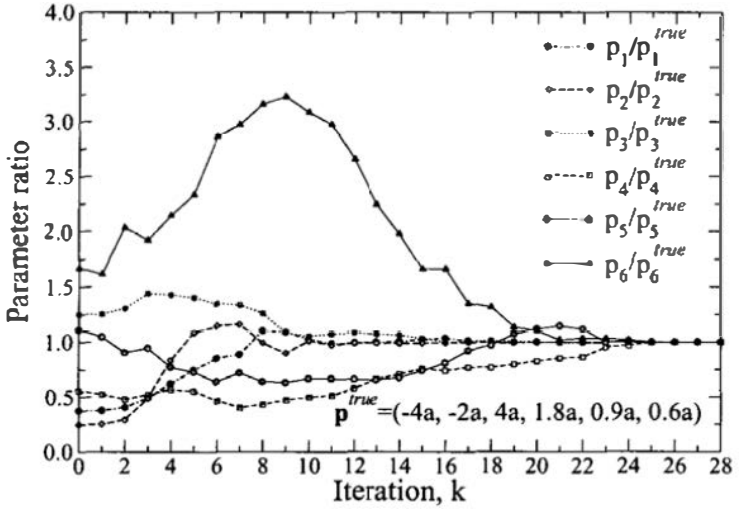

Figure 1. Evolution of design parameters in the minimization process.

$i = 1, 2, 3$ so that $\boldsymbol{p} = (c_1, c_2, c_3, \alpha_1, \alpha_2, \alpha_3)$. The cavity is illuminated in succession via nine point sources with respective magnitude $P = 0.2\mu a^2$. The testing configuration is a grid with 64 receivers. The shear wave length λ_s is approximately twice the diameter d of the cavity. As can be seen from Fig. 1, the iterative procedure converges after roughly 25 major iterations.

It should be noted, however, that the success of the foregoing method is strongly dependent on the choice of the starting point, a pitfall that is common to all gradient-based algorithms. This consideration led the authors to investigate the usefulness of the concept of *topological derivative* [3,9,4,6] in connection with the elastodynamic inverse problem.

Topological derivative. To search the semi-infinite domain Ω for cavities in the context of (3), let $B_a(x^o) = x^o + a\mathcal{B}$ define the cavity of size $a > 0$ and volume $a^3\,|\mathcal{B}|$, where $\mathcal{B} \subset \mathbb{R}^3$ is a *fixed* and bounded open set of volume $|\mathcal{B}|$ containing the origin. Without loss of generality, $\mathcal{B}$ is chosen so that $B_a(x^o)$ is contained inside the sphere of radius a centered at x^o. With such definitions, the topological derivative of (3) can be defined as

$$\mathcal{T}(x^o) = \lim_{a \to 0} \; (a^3\,|\mathcal{B}|)^{-1} \left[\mathcal{J}(\Omega \backslash \overline{B}_a) - \mathcal{J}(\Omega) \right], \qquad x^o \in B_a, \qquad (6)$$

which furnishes the information about the variation of $\mathcal{J}(\Omega)$ if a hole of prescribed shape $\mathcal{B}$ and infinitesimal characteristic size is created at $x^o \in \Omega$. Within the framework of shape optimization, it was shown [9,4] that the

elastostatic equivalent of (6) can be used as a powerful tool for the grid-based exploration of a solid for plausible void regions for a given functional $\mathcal{J}$. Here, this concept will be extended to elastic-wave imaging of semi-infinite solids on the basis of the elastodynamic fundamental solution for a homogeneous isotropic half-space.

In the present context, the topological derivative $\mathcal{T}(\boldsymbol{x}^o)$ defined by (6) is found to be given by

$$\mathcal{T}(\boldsymbol{x}^o) = \sum_{m=1}^{M} \mathrm{Re}\Big[\{\overline{\boldsymbol{u}^{\mathrm{F}}(\boldsymbol{x}^m) - \boldsymbol{u}^{\mathrm{obs}}(\boldsymbol{x}^m)}\}\cdot \boldsymbol{W}^m \cdot \boldsymbol{e}_k \Big(\hat{\boldsymbol{\sigma}}^k(\boldsymbol{x}^o, \boldsymbol{x}; \omega) : \boldsymbol{\mathcal{A}} : \boldsymbol{\sigma}^{\mathrm{F}}(\boldsymbol{x}^o) - \rho^2 \hat{\boldsymbol{u}}^k(\boldsymbol{x}^o, \boldsymbol{x}; \omega)\cdot \boldsymbol{u}^{\mathrm{F}}(\boldsymbol{x}^o)\Big)\Big] \quad (7)$$

where the constant tensor $\boldsymbol{\mathcal{A}}$ depends in a known way on the shape of the infinitesimal cavity. When this shape is spherical, one has

$$\boldsymbol{\mathcal{A}} = \frac{3(1-\nu)}{2\mu(7-5\nu)}\Big[5\,\mathbf{I}_4^{sym} - \frac{1+5\nu}{2(1+\nu)}\mathbf{I}_2 \otimes \mathbf{I}_2\Big]$$

and (7) is consistent with that given in Ref. 4 for elastostatic problems.

Numerical example. The configuration is as depicted in Fig. 2. The 'true' spherical cavity, of diameter $D = 0.4d$, is centered at $(d, 0, 3d)$ inside the half-space. In succession, the cavity is illuminated by sixteen axial point sources acting on the surface of a semi-infinite solid; for each source location, Cartesian components of the ground motion, $\boldsymbol{u}^{\mathrm{obs}}$, are monitored via twenty five sensors distributed over the square testing grid; here, this data is simulated using the BEM formulation of the forward problem. BEM. Four excitation frequencies $\bar{\omega} \equiv \omega d\sqrt{\rho/\mu} = 1, 2, 4, 8$ have been considered.

For this testing configuration, the values of $\mathcal{T}(\boldsymbol{x}^o)$ are computed over the horizontal surface $S_h = \{\boldsymbol{\xi} \in \Omega \mid -5d < \xi_1 < 5d,\ -3d < \xi_3 < 3d,\ \xi_3 = 3d\}$

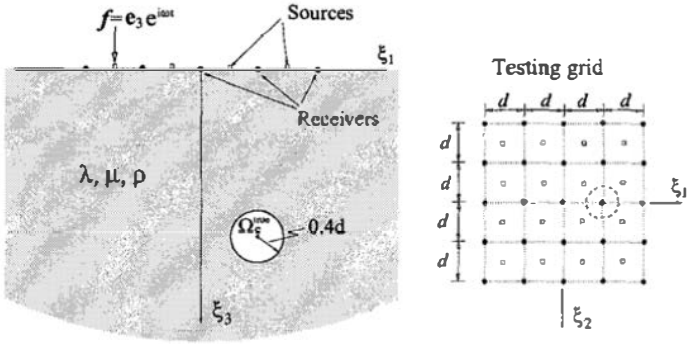

Figure 2. Sample imaging problem.

passing through the centroid of the 'true' cavity and plotted in Fig. 3 for the above-defined set of frequencies. The computational grid is chosen so that the sampling points x^o are spaced by $0.25d$ in both ξ_1 and ξ_2 directions. In the display, the red tones indicate negative values of $\mathcal{T}$ and thus possible cavity location; for comparison, the true cavity is outlined in white in each of the diagrams. The results clearly demonstrate the usefulness of the topological derivative as a computationally efficient tool for exposing the approximate cavity location, with "higher" frequencies ($\bar{\omega} = 2, 4$) providing in general better resolution. From the diagram for $\bar{\omega} = 8$ where $\lambda_s/D \approx 1$, however, it is also evident that the infinitesimal-cavity assumption embedded in (7) performs best when used in conjunction with wave lengths exceeding the cavity diameter.

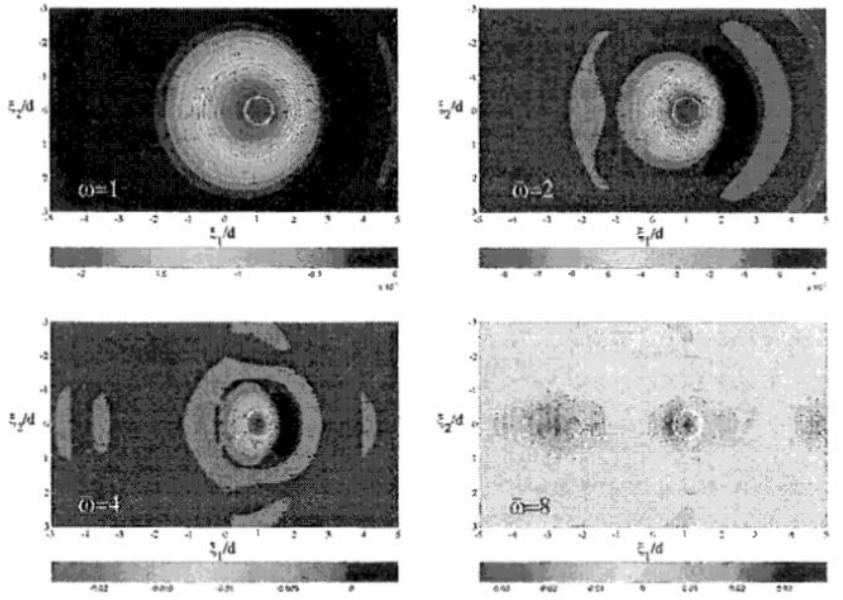

Figure 3. Distribution of $(\mu d)^{-1}\mathcal{T}(x^o)$ in the $\xi_3 = 3d$ (horizontal) plane.

For completeness, the variation of $\mathcal{T}(x^o)$ across the vertical planar region $S_v = \{\xi \in \Omega | -5d < \xi_1 < 5d, \xi_2 = 0, 0.25d < \xi_3 < 6d\}$ is given in Fig. 4. Similar to the earlier diagram, the sampling points x^o are spaced by $0.25d$ in the ξ_1 and ξ_3 directions. A diminished resolution relative to the previous result reflects the major limitation of the 'experimental' data set, that is, the fact that both source and receiver points are limited to a single planar surface. The contour plots for $\bar{\omega} = 2$ and 4 exhibit greater

accuracy than that for $\bar{\omega} = 1$, but are also plagued with local minima that are absent in the former diagram. The non-informative distribution of $\mathcal{T}$ for $\bar{\omega} = 8$ indicates that the use of topological derivative in elastic-wave imaging is most effective at 'low' excitation frequencies, i.e. those inside the resonance region.

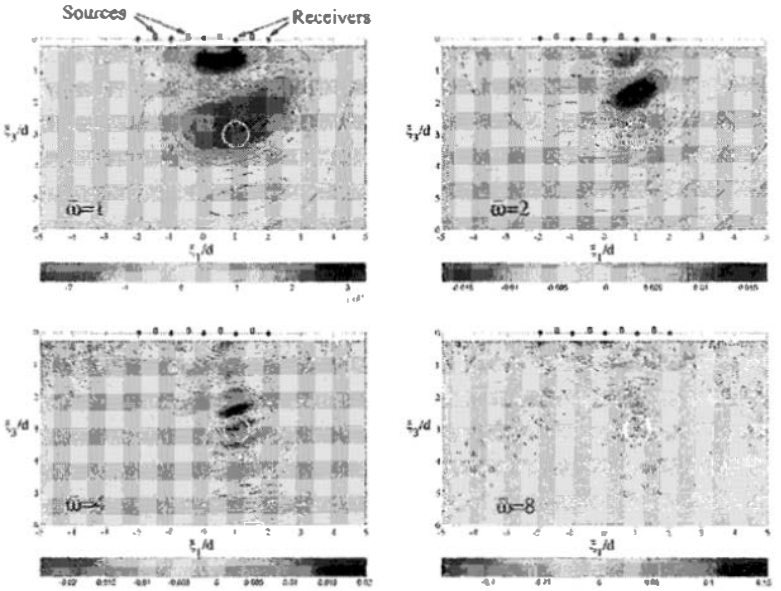

Figure 4. Distribution of $(\mu d)^{-1}\mathcal{T}(\boldsymbol{x}^o)$ in the $\xi_2 = 0$ (vertical) plane.

With diagrams such as those in Figs. 3 and 4, an algorithm for identifying plausible cavity locations could be devised on the basis of the non-zero distribution of an auxiliary function

$$\overset{*}{\mathcal{T}}(\boldsymbol{x}^o) = \begin{cases} \mathcal{T}(\boldsymbol{x}^o), \mathcal{T} < C, \\ 0, \quad \mathcal{T} \geq C, \end{cases} \tag{8}$$

with a suitable threshold value $C < 0$. With such definition, it is also possible to combine the individual advantages of different probing wavelengths by employing the product of (8) at several frequencies. As an illustration of the latter approach, Fig. 5 plots the distribution of the product of $\overset{*}{\mathcal{T}}|_{\bar{\omega}=1}$ and $\overset{*}{\mathcal{T}}|_{\bar{\omega}=2}$ in the vertical plane, with C set to approximately 40% of the global minima of the respective distributions in Fig. 4. Despite the limited accuracy and multiple minima characterizing respectively the individual solutions for $\bar{\omega} = 1$ and $\bar{\omega} = 2$, the combined result stemming from (8) points

to a single cavity with its centre and size closely approximating the true void configuration.

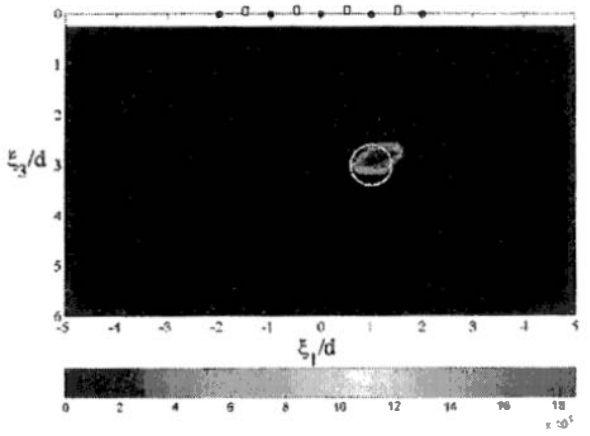

Figure 5. Distribution of $(\mu d)^{-2}\,\mathring{T}|_{\bar{\omega}=1} \times \mathring{T}|_{\bar{\omega}=2}$ in the $\xi_2 = 0$ plane.

References

1. BONNET, M. BIE and material differentiation applied to the formulation of obstacle inverse problems. *Eng. Anal. with Bound. Elem.*, **15**, 121–136 (1995).
2. COLTON, D., KRESS, R. *Integral Equation Method in Scattering Theory*. Wiley, New York (1983).
3. ESCHENAUER, H. A., KOBELEV, V. V., SCHUMACHER, A. Bubble method for topology and shape optimization of structures. *Structural Optimization*, **8**, 42–51 (1994).
4. GARREAU, S., GUILLAUME, P., MASMOUDI, M. The Topological Asymptotic for PDE Systems: The Elasticity Case. *SIAM J. Control Optim.*, **39**, 1756–1778 (2001).
5. GUZINA, B. B., NINTCHEU FATA, S., BONNET, M. On the stress-wave imaging of cavities in a semi-infinite solid. *Int. J. Solids Struct.*, **40**, 1505–1523 (2003).
6. GUZINA, B. B., BONNET, M. Topological derivative for the inverse scattering of elastic waves. *Quart. J. Mech. Appl. Math.*, to appear (2003).
7. NINTCHEU FATA, S., GUZINA, B. B., BONNET, M. A computational basis for elastodynamic cavity identification in a semi-infinite solid. *Comp. Mech.*, to appear (2003).
8. PAK, R. Y. S., GUZINA, B. B. Seismic soil-tructure interaction analysis by direct boundary element methods. *Int. J. Solids Struct.*, **36**, 4743–4766 (1999).
9. SOKOLOWSKI, J., ZOCHOWSKI, A. On the topological derivative in shape optimization. *SIAM J. Control Optim.*, **37**, 1251–1272 (1999).